SCIENTIFIC REP♦RTS

OPEN

B-site ordering and strain-induced phase transition in double-perovskite La$_2$NiMnO$_6$ films

Sheng-Qiang Wu[1], Sheng Cheng[2], Lu Lu[2], Ming Liu[2], Xiao-Wei Jin[2], Shao-Dong Cheng[1,2] & Shao-Bo Mi[1]

The magnetic and electrical properties of complex oxide thin films are closely related to the phase stability and cation ordering, which demands that we understand the process-structure-property relationships microscopically in functional materials research. Here we study multiferroic thin films of double-perovskite La$_2$NiMnO$_6$ epitaxially grown on SrTiO$_3$, KTaO$_3$, LaAlO$_3$ and DyScO$_3$ substrates by pulsed laser deposition. The effect of epitaxial strains imposed by the substrate on the microstructural properties of La$_2$NiMnO$_6$ has been systematically investigated by means of advanced electron microscopy. It is found that La$_2$NiMnO$_6$ films under tensile strain exhibit a monoclinic structure, while under compressive strain the crystal structure of La$_2$NiMnO$_6$ films is rhombohedral. In addition, by optimizing the film deposition conditions a long-range ordering of B-site cations in La$_2$NiMnO$_6$ films has been obtained in both monoclinic and rhombohedral phases. Our results not only provide a strategy for tailoring phase stability by strain engineering, but also shed light on tuning B-site ordering by controlling film growth temperature in double-perovskite La$_2$NiMnO$_6$ films.

Double-perovskite multiferroic La$_2$NiMnO$_6$ (LNMO) received much attention in recent decades due to its abundant magnetoresistance, magnetocapacitance[1–3] and dielectric properties[2,4,5]. In particular, the near room temperature magnetic properties have opened up a wealth of promising applications in ferromagnetic semiconductor for spintronics and magnetoelectronics[6–8]. For LNMO materials, chemical ordering of B-site cations (Ni/Mn) strongly affects physical properties, particularly magnetic properties[5,7,9–11]. B-site ordered LNMO shows a single paramagnetic-to-ferromagnetic curie temperature (about 280 K) due to the Ni^{2+}-O-Mn^{4+} superexchange interaction[6,12]. In contrast, for B-site disordered LNMO, Ni-O-Ni and Mn-O-Mn bonds are believed to have antiferromagnetic superexchange interactions[6,13,14]. Additionally, ordering of B-site cations affects crystal structure of LNMO. It was reported that orthorhombic LNMO (*Pbnm*) is B-site disordered and monoclinic LNMO (*P2$_1$/n*) exhibits a long-range B-site ordering[15–18]. For epitaxial films, it is important to note that synthetic conditions such as film-growth temperature and oxygen pressure could affect crystal structure and physical properties of the films[7,19–22], e.g. BaTiO$_3$ films grown on SrTiO$_3$ substrates at different oxygen partial pressures[21]. Particularly, B-site ordering in double-perovskite films could be influenced by oxygen partial pressure, e.g. La$_2$CoMnO$_6$[23] and La$_2$NiMnO$_6$[19,24]. It should be noted that the ordering of B-site cations in the double-perovskite films could be improved by controlling the growth temperature, e.g. La$_2$CuSnO$_6$ films[25].

In addition, the epitaxial strain of thin films affects the microstructural and physical properties of the films[26–35]. R. J. Zeches *et al.*[28] reported that strain-driven phase evolution occurs in multiferroic BiFeO$_3$ films by controlling the epitaxial strain imposed by the substrate. For the double-perovskite Y$_2$NiMnO$_6$ films[27], the magnetic properties and the related ferromagnetic transition temperature (T_c) show a strong dependence on the biaxial tensile strain in the films. It is noted that in comparison with the significant studies on the synthesis and properties of bulk materials[1,6,13,18,36,37], there was a lack of information on the ordering of B-site in double-perovskite films related to the growth parameters and the epitaxial strain induced structure evolution. In our previous work, the short-range ordering of the B-site cation was obtained in the LNMO films coherently grown on the perovskite-type STO and LSAT substrates at 800 °C[26]. Nevertheless, phase stability of LNMO films related to the strain relaxation and the effect of film-growth temperature on the chemical ordering of B-site cations in LNMO films are less concerned.

[1]State Key Laboratory for Mechanical Behavior of Materials, Xi'an Jiaotong University, Xi'an, 710049, China. [2]School of Microelectronics, Xi'an Jiaotong University, Xi'an, 710049, China. Correspondence and requests for materials should be addressed to S.-B.M. (email: shaobo.mi@xjtu.edu.cn)

Nowadays, based on aberration-corrected electron microscopy, advanced imaging techniques in combination with atomic-resolution energy-dispersive X-ray spectroscopy (EDS) mapping provide us with unrivaled capability to understand the structural and chemical properties of materials at the atomic scale[38–44]. In this work, by applying these microscopic analytical techniques, we have systematically investigated phase structure of LNMO films affected by the epitaxial strain and misfit strain relaxation of LNMO films grown on different perovskite-type substrates including $KTaO_3$ (KTO), $DyScO_3$ (DSO), $SrTiO_3$ (STO) and $LaAlO_3$ (LAO). We have also studied the effect of film-growth temperature on the ordering of B-site cation in LNMO films. We hope that the present studies would promote the understanding of the effect of the growth process on the structural and physical properties in double-perovskite LNMO films.

Results and Discussion

It is well known that STO and KTO have a cubic perovskite-type structure with a lattice parameter of 0.3905 and 0.3988 nm at room temperature[45,46], respectively. In contrast, LAO has a rhombohedrally distorted perovskite-type structure[47], and DSO has an orthorhombically distorted perovskite-type structure at room temperature[48]. To simplify the discussion, LAO and DSO can be treated as a pseudocubic structure with a lattice parameter (a_p) of 0.3791 nm and 0.3952 (0.3957 nm) nm, respectively, where the subscript P denotes a pseudocubic perovskite-type structure.

Figure 1a–c are low-magnification bight-field transmission electron microscopy (BF-TEM) images, showing an overview of LNMO films grown on (001) STO, (001) KTO and $(001)_p$ DSO substrates, respectively. The contrast variation is clearly visible in the LNMO films, which allows us to locate the film-substrate interface, as indicated by horizontal white arrows. A typical selected area electron diffraction (SAED) pattern of the LNMO/KTO heterostructure is displayed in Fig. 1d, viewed along the [010] KTO zone axis. A vertical white arrow shows the splitting of diffraction spots between LNMO and KTO, indicating that the relaxation of misfit strain occurs between LNMO film and KTO substrate. In addition, weak diffraction spots from LNMO films but different oriented domains are presented, as denoted by a blue and a red arrow. It should be noted that the weak reflections also appear in the SAED patterns of LNMO film grown on STO and DSO substrates (See Figure S1 of the Supplemental Material). The appearance of weak reflections in the diffraction patterns means that LNMO films have a monoclinic or an orthorhombic structure. It should be mentioned that monoclinic LNMO ($P2_1/n$) and orthorhombic LNMO ($Pbnm$) display structural similarity, which leads to impossible to discern them based on X-ray measurement[17] and SAED patterns. In contrast to the coherent growth of LNMO films on (001) STO substrate, misfit dislocations are observed at the LNMO/KTO and LNMO/DSO interfaces. Figure 1e shows a typical high-resolution high-angle annular dark field (HAADF) image containing a misfit dislocation at the LNMO/KTO interface, viewed along [010] KTO zone axis. The LNMO/KTO interface is denoted by a horizontal red arrow. It is found that the misfit dislocation has a projected Burgers vector of $a<100>$ (a is the lattice parameter of KTO), which is obtained by performing a Burgers circuit around the dislocation core, as shown in Fig. 1e.

Figure 2a is a low-magnification TEM image of 8-nm-thick LNMO films grown on $(001)_p$ LAO substrate, viewed along the $[010]_p$ LAO zone-axis. No misfit dislocations are observed at the LNMO/LAO interface, indicating the LNMO films coherently grow on the LAO substrate. In contrast, for the 100-nm-thick LNMO films grown on $(001)_p$ LAO substrates, the contrast variation is present within the LNMO films, as shown in a low-magnification BF-TEM image in Fig. 2b. The thick LNMO films exhibit a bilayer structure (referred as $LNMO_L$ and $LNMO_H$ respectively). The interface between $LNMO_L$ and $LNMO_H$ is indicated by a horizontal white arrow. The $LNMO_L$ layer coherently grows on the LAO substrate with a thickness of about 30 nm. The layer displays a uniform contrast, indicating that it is a monodomain. In comparison, a high density of dark diffuse lines can be seen in the $LNMO_H$ layer, starting from the $LNMO_L/LNMO_H$ interface and penetrating in most cases the whole $LNMO_H$ layer. Figure 2c shows the SAED pattern of the LNMO/LAO heterostructure. No weak diffraction spots from $LNMO_L$ and $LNMO_H$ are observed, which indicates that both LNMO layers have a rhombohedral structure. The splitting of diffraction spots can be observed obviously for the high-index reflections. The inset shows the reflection around 402_{LAO} as denoted by a white rectangle in Fig. 2c. It can be seen that there is no in-plane relaxation between LAO and $LNMO_L$, which results in that the $LNMO_L$ layer has a larger out-of-plane lattice parameter (0.398 ± 0.002 nm). In contrast, in-plane relaxation occurs between $LNMO_H$ and $LNMO_L$ since the in-plane splitting of reflections can be clearly detected. The epitaxial strain between $LNMO_H$ and $LNMO_L$ is relaxed by the formation of misfit dislocation at the interface, as shown in Fig. 2d. The projected Burgers vector of the misfit dislocation is $a_p<100>$ (a_p is the lattice parameter of the pseudocubic LNMO), which is obtained by drawing a Burgers circuit around the dislocation core.

It is noted that both LAO and LNMO have a rhombohedral structure in the LNMO/LAO system, which might be in favor of monodomain LNMO films ($LNMO_L$) coherently grown on the LAO substrates below a critical thickness. Accordingly, the large compressive strain is accommodated by the elastic deformation of the lattice. Furthermore, with increasing LNMO film thickness above the critical thickness (~30 nm), the film growth mechanism might change from layer-by-layer (Frank-van der Merve mode) growth to island growth to release the large in-plane compressive strain, which results in the formation of the $LNMO_H$ layer on the $LNMO_L$ layer. Meanwhile, at the $LNMO_H/LNMO_L$ interface misfit dislocations appear due to the coalescence of the $LNMO_H$ nuclei during the film growth, which contributes to misfit strain relaxation in the LNMO/LAO system.

To understand the structural properties at the LNMO/LAO interface, high-resolution HAADF investigations of the interface have been performed. A typical atomic-resolution HADDF image of the LNMO/LAO interface is shown in Fig. 3a, viewed along the $[010]_p$ LAO zone axis. It is noted that the intensity of atomic columns in the HAADF image is roughly proportional to Z^2 (where Z is the atomic number averaged in the atomic columns)[49]. The interfacial (Ni, Mn)O_2 and AlO_2 layer can be located, as indicated by a horizontal red and a horizontal green arrow, respectively. To obtain the chemical information of B-site cations across LNMO/LAO interface, Fig. 3b displays intensity profiles along the atomic plane marked by a red line in Fig. 3a. Obviously, the intensity
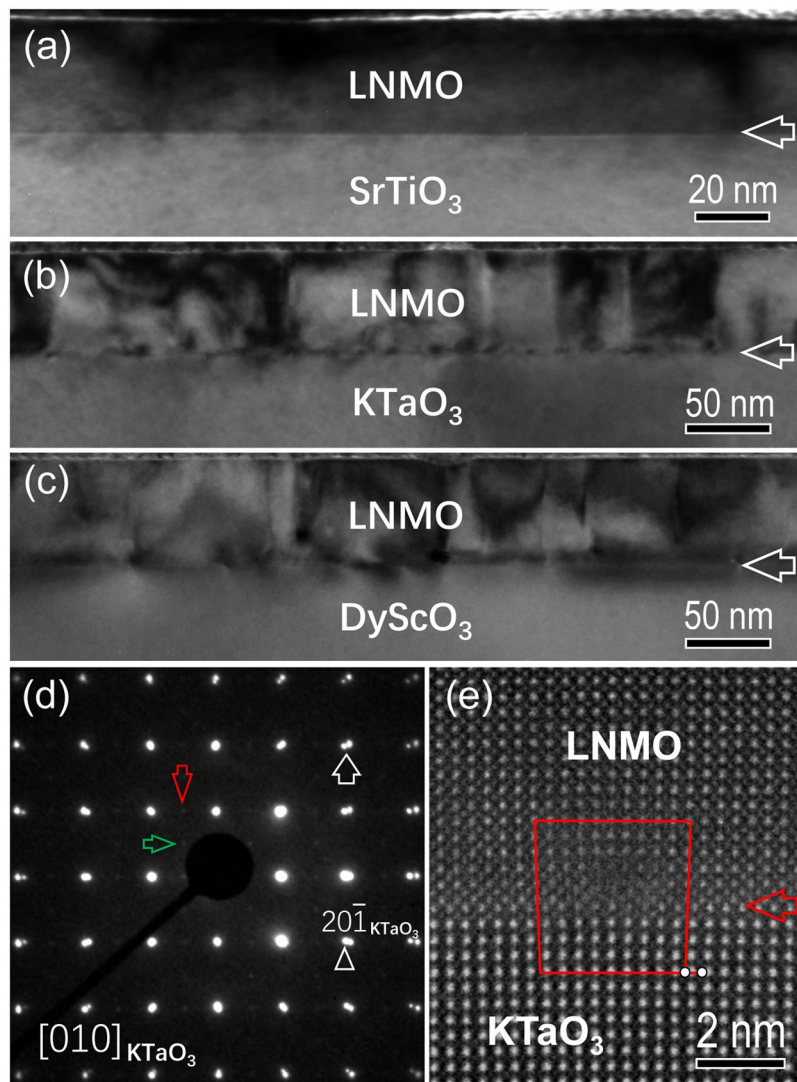
Figure 1. (**a–c**) Low-magnification BF-TEM image of the LNMO/STO, LNMO/KTO and LNMO/DSO heterostructures, respectively, viewed along the [010] zone axis of the substrate. The horizontal white arrow denotes the film-substrate interface. (**d**) The SAED pattern from the LNMO/KTO heterostructure, viewed along the [010] KTO zone axis. The splitting of diffraction spots between KTO and LNMO is indicated by a vertical white arrow. The weak diffraction spot from different domains of the LNMO films is denoted by a blue and a red arrow, respectively. (**e**) High-resolution HAADF image showing misfit dislocations at the LNMO/KTO interface. The interface is indicated by a horizontal red arrow.

of interfacial Al−O columns is higher than that of other Al−O columns, implying that the interface diffusion may occur between Al and Ni/Mn. The out-of-plane lattice parameters in the interface area have been investigated by geometrical lattice mapping directly on the high-resolution HAADF image using a 2D Gaussian fitting approach[50,51]. Figure 3c displays a plot of the out-of-plane lattice spacing against the distance, which provides evidence for the difference in the out-of-plane lattice parameters between LNMO and LAO across the interface.

It is known that B-site ordered LNMO displays ferromagnetic properties due to the Ni-O-Mn interaction. In contrast, apart from Ni-O-Mn superexchange interaction the Mn-O-Mn and Ni-O-Ni antiferromagnetic couplings occur in the short-range B-site ordered LNMO[15]. The ordering of B-site cations (Ni and Mn) in our LNMO films has been investigated by atomic-resolution energy-dispersive X-ray spectroscopy (EDS) mapping. The B-site ordering can be distinguished from the $<110>_P$ direction of pseudocubic LNMO, as a schematic model illustrated in Fig. 4a. Figure 4b shows a typical high-resolution HAADF image of LNMO films, viewed along the $[110]_P$ LNMO zone axis. Atomic-resolution EDS mapping for Mn and Ni is displayed in Fig. 4c and d, respectively, which shows a long-range ordering of Ni and Mn in LNMO. It was reported that in contrast to the orthorhombic phase, the monoclinic phase of LNMO is B-site cations ordered[17]. Thus, under our LNMO film-growth conditions, the monoclinic LNMO phase has been obtained. In addition, in contrast to the short-range B-site ordered LNMO films grown at 800 °C (See Figure S2 of the supplemental material), both rhombohedral and monoclinic LNMO films display a long-range B-site ordering at 900 °C (See Figure S3 of the Supplemental Material).
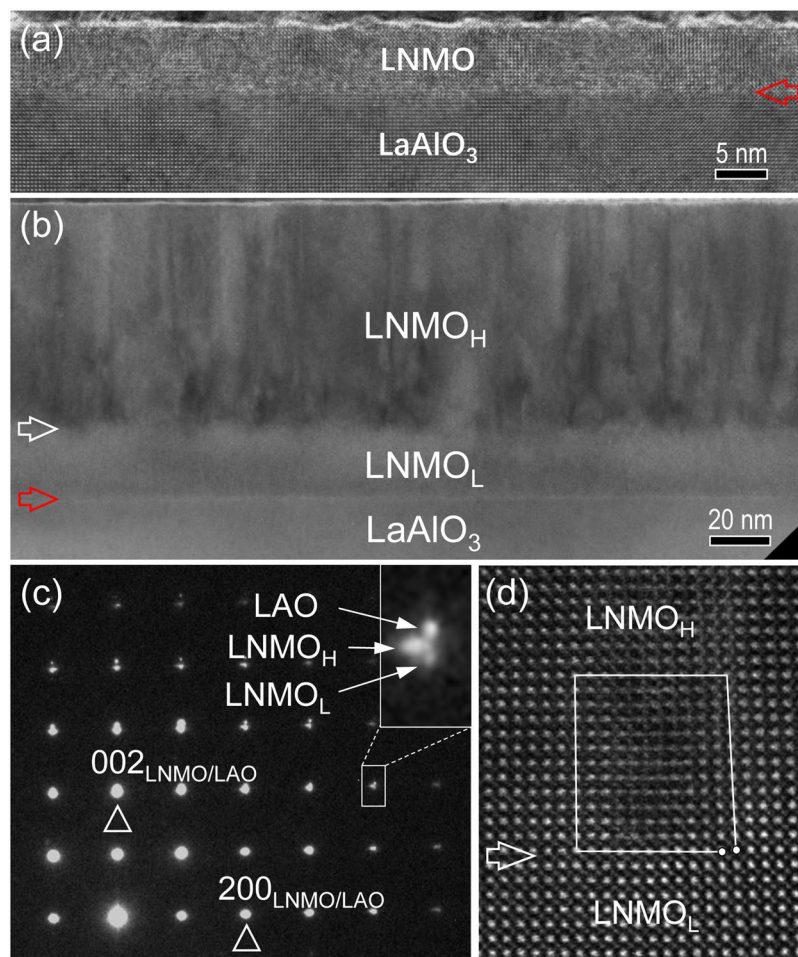
Figure 2. Low-magnification BF-TEM image of the LNMO/LAO heterostructures with 8-nm-thick (**a**) and 100-nm-thick (**b**) LNMO films, respectively. The LNMO/LAO interface is indicated by a horizontal red arrow. The LNMO$_L$/LNMO$_H$ and LNMO$_L$/LAO interface is indicated by a horizontal white and a horizontal red arrow, respectively. (**c**) The SAED pattern recorded in the region of the LAO substrate and 100-nm-thick LNMO films, viewed along the $[010]_p$ LAO zone-axis. The insert shows the separation of the reflection spot of LNMO$_L$, LNMO$_H$ and LAO. (**d**) High-resolution HAADF image of misfit dislocations at the LNMO$_L$/LNMO$_H$ interface. The interface is denoted by a white arrow.

It should be mentioned that bond length and bond angle of Ni^{2+}-O-Mn^{4+} in the B-site ordered monoclinic and rhombohedral LNMO should be essentially different, which affects the superexchange interactions and the related physical properties (e.g. ferromagnetic) of the films.

In addition, applying atomic-resolution EDS mapping the chemical composition of the LNMO/LAO and LNMO/STO heterointerface has been investigated. Figure 4e shows a high-resolution HAADF image of the LNMO/LAO interface. The corresponding EDS map for Al, Mn and Ni is displayed in Fig. 4f–h, respectively. A monolayer interdiffusion between Mn/Ni and Al was observed at the interface, as indicated by a horizontal white arrow. It can be seen that the rhombohedral LNMO films also exhibit a long-range B-site ordering at the interface area. A high-resolution HAADF image of the LNMO/STO interface is shown in Fig. 4i. The EDS map of B-site cations at the interface is shown in Fig. 4j–l, respectively. The interfacial Ti-O layer is indicated by a horizontal white arrow. Slight interdiffusion between Mn/Ni and Ti occurs at the interface. Also, B-site cations in LNMO display a long-range ordering at the LNMO/STO interface area.

To understand the phase stability of LNMO films, we calculated misfit strain between LNMO films and a variety of substrates, as shown in Table 1. In fact, the unit cell parameters of double-perovskite LNMO structure[52] can be related to an ideal ABO$_3$ perovskite-type unit cell. The monoclinic LNMO has lattice parameters $a = 5.467$ Å, $b = 5.510$ Å ($a_{P1} \approx a_{P2} \approx \sqrt{a^2 + b^2}/2 \approx 3.881$ Å), $c = 7.751$ Å ($a_{P3} = c/2 \approx 3.875$ Å), and $\beta = 90.12°$, where a_{P1}, a_{P2} and a_{P3} are pseudocubic unit-cell lengths. The rhombohedral LNMO has lattice parameters a $= 5.475$ Å ($a_{P1} = a_{P2} = a_{P3} \approx a/\sqrt{2} \approx 3.871$ Å), and $\beta = 60.67°$. In the case of the monoclinic LNMO on the substrates, several types of film-substrate orientation relationship may exist depending on the crystallographic structure of the substrate, e.g. O$_1$, O$_2$ and O$_3$ in the LNMO/DSO system, which leads to different in-plane strains in the two orthogonal directions. Also, anisotropic in-plane strain may occur in the rhombohedral LNMO because of the substrate with different in-plane lattice parameters, e.g. in the LNMO/DSO system. As list in the Table 1, both
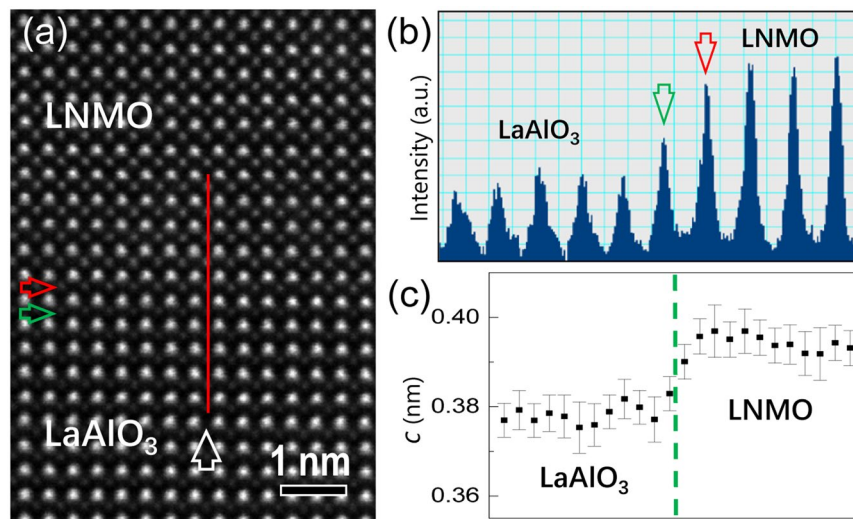
Figure 3. (**a**) Atomic-resolution HAADF image of the LNMO/LAO interface, viewed along the $[010]_p$ LAO zone axis. The interfacial $(Ni, Mn)O_2$ and AlO_2 layer is denoted by a horizontal red and a horizontal green arrow, respectively. (**b**) The intensity profiles along the red line in Fig. 3a, showing the intensity variation of B-site cation columns in LNMO and LAO across the interface. (**c**) The value of the out-of-plane lattice parameter (*c*) across the LNMO/LAO interface.

monoclinic and rhombohedral LNMO films undergo tensile strain if the films coherently grow on STO, DSO and KTO. Nevertheless, in-plane mismatch strain of monoclinic LNMO is smaller than that of rhombohedral LNMO. In contrast, although compressive epitaxial strain would be induced in both monoclinic and rhombohedral LNMO films if the films coherently grow on LAO, (001) (La, Sr)(Al,Ta)O_3 (LSAT) ($Pn\bar{3}m$)[53] and (001) LaSrAlO_4 (LSAO) ($I4/mmm$)[54], in-plane mismatch strain of monoclinic LNMO is larger than that of rhombohedral LNMO. The different in-plane mismatch strain possibly results in the formation of monoclinic LNMO films under the tensile strain and rhombohedral LNMO films under the compressive strain. The relationship of strain-induced phase transition in LNMO films is shown in Fig. 5.

According to our experimental results, the small lattice mismatch could be fully accommodated by the elastic deformation of the lattice and oriented domains, which leads to the coherent growth of films on substrates, e.g. in the LNMO/STO and LNMO/LSAT systems[26]. In most cases, with the increase of the film-substrate lattice mismatch, apart from the formation of oriented domains in the LNMO films misfit dislocations appear at the film-substrate interface, contributing to misfit strain relaxation. As a result, the films and the substrates form the semi-coherent interface, e.g. in the LNMO/DSO and LNMO/KTO systems. It is important to note that both coherently and semi-coherently strained LNMO films under the tensile strain exhibit a monoclinic structure and under the compressive strain a rhombohedral structure.

Additionally, in comparison with the partially disordered LNMO films grown at 800 °C[26], the LNMO films prepared at 900 °C exhibit a long-range B-site ordering. In fact, with the exception of the growth temperature, the deposition conditions were held the same for preparing LNMO films in these two works. In other words, our works indicate that B-site ordering in LNMO films could be improved efficiently by increasing growth temperature. It is noted that the growth temperature can significantly influence the film growth kinetics, e.g. the thermal diffusion of the cations in the lattice[55–57]. Increasing film-growth temperature increases the kinetic energy of the diffusing cations in the LNMO, which could lead the B-site cations (Ni and Mn) to arrange themselves in the cation sublattice in an ordered manner. In fact, the ordering of B-site in bulk LNMO could be improved by changing the thermal annealing parameters[24]. In this viewpoint, post-growth annealing of the LNMO films may provide an alternative way of manipulating the B-site ordering in order to enhance their performance in device applications.

Conclusions

In summary, by means of advanced electron microscopy we have demonstrated that the misfit strain of LNMO films grown on different substrates could be partially released by the formation of oriented domains within the films and misfit dislocations at the interfaces. Importantly, phase stability of LNMO films could be tuned effectively by elastic strains imposed by the substrate. Under tensile stain, LNMO films exhibit a monoclinic structure, while under compressive strain LNMO films are rhombohedral. In addition, a long-range B-site ordered LNMO films have been successfully prepared at 900 °C. Our work indicates that the ordering of B-site cations in LNMO films could be affected by controlling film-growth temperature. Importantly, the atomic-scale characterization of chemical and structural properties of double-perovskite multiferroic LNMO films would extend our understanding of the process-structure-property relationship in the materials and explore their potential applications.
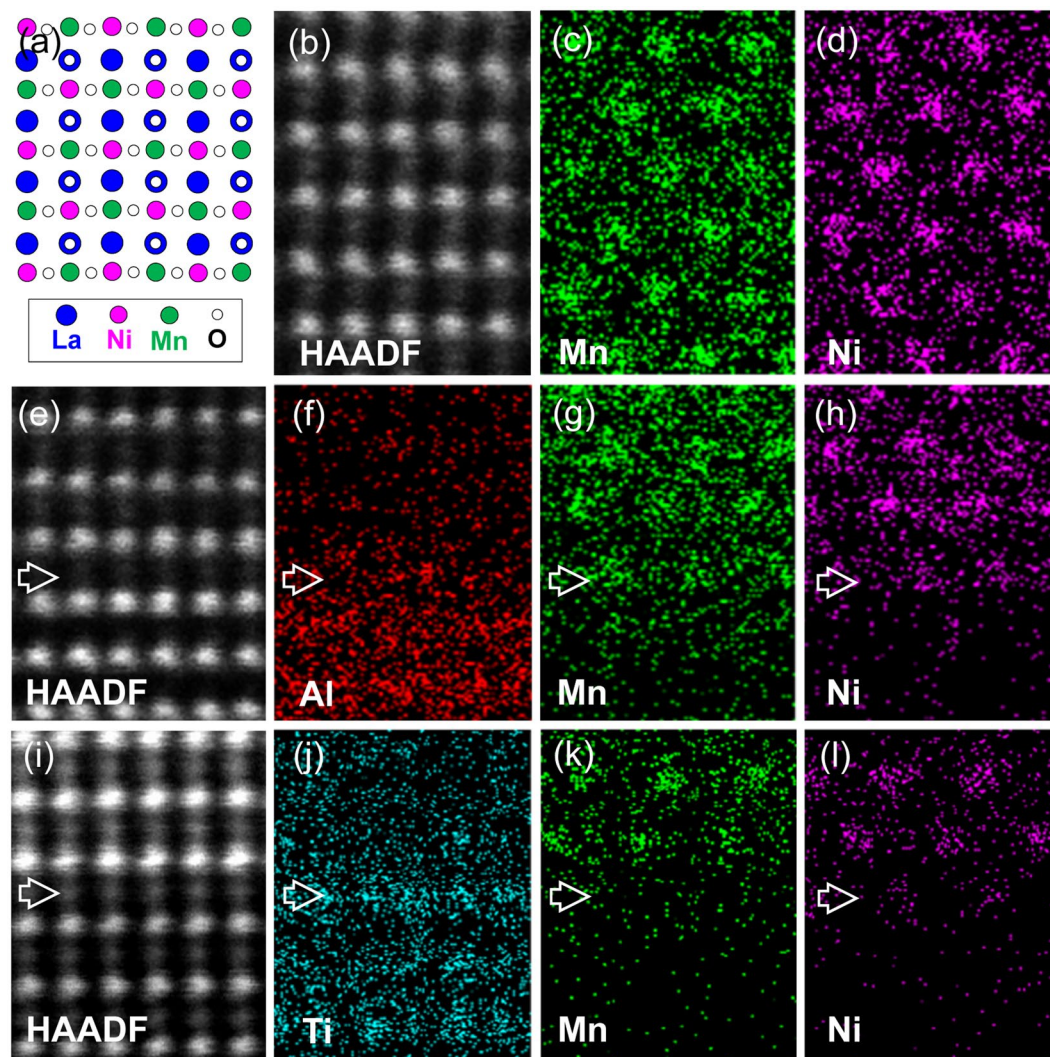
Figure 4. (**a**) Schematic structure model of B-site ordered LNMO, viewed along $<110>_p$ LNMO zone axis. (**b–d**) Atomic-resolution HAADF image of LNMO films and EDS maps of Mn and Ni. (**e–h**) HAADF image of the LNMO/LAO interface and EDS maps of Al, Mn and Ni. (**i–l**) HAADF image of the LNMO/STO interface and EDS maps of Ti, Mn and Ni.

Materials	Crystal structure	Unit cell lattice parameters (Å)			Pseudocubic lattice parameters (Å)			In-plane lattice mismatch (with Monoclinic LNMO)		In-plane lattice mismatch (with Rhombohedral LNMO)	
		a	b	c	a_{P1}	a_{P2}	a_{P3}	Δf_{M1}	Δf_{M2}	Δf_{R1}	Δf_{R2}
LNMO	$R\bar{3}$	5.475	5.475	5.475	3.871	3.871	3.871				
LNMO	$P2_1/n$	5.467	5.510	7.751	3.881	3.881	3.875				
KTO	$Pm\bar{3}m$	3.988	3.988	3.988				−2.68%	−2.83%	−2.93%	−2.93%
DSO	$Pbnm$	5.449	5.726	7.913	3.952	3.952	3.957	−1.80% (O_1) −1.92% (O_2) −1.80% (O_3)	−1.92% (O_1) −1.95% (O_2) −2.07% (O_3)	−2.05%	−2.17%
STO	$Pm\bar{3}m$	3.905	3.905	3.905				−0.61%	−0.77%	−0.87%	−0.87%
LSAT	$Pn\bar{3}m$	7.720	7.720	7.720	3.860	3.860	3.860	0.54%	0.39%	0.28%	0.28%
LAO	$R\bar{3}$	5.360	5.360	13.086	3.791	3.791	3.791	2.37%	2.22%	2.11%	2.11%
LSAO	$I4/mmm$	3.754	3.754	12.649				3.38%	3.22%	3.12%	3.12%

Table 1. Crystal structure and lattice parameter of STO (ref.[45]), KTO (ref.[46]), LAO (ref.[47]), DSO (ref.[48]), LSAT (ref.[53]), and LSAO (ref.[54]) substrates, and the in-plane lattice mismatch between LNMO (ref.[52]) and various substrates, which is calculated by using the equation of $\Delta f = (a_f - a_0)/a_0 * 100\%$ (a_0 and a_f are the lattice parameter of substrate and pseudocubic LNMO, respectively).
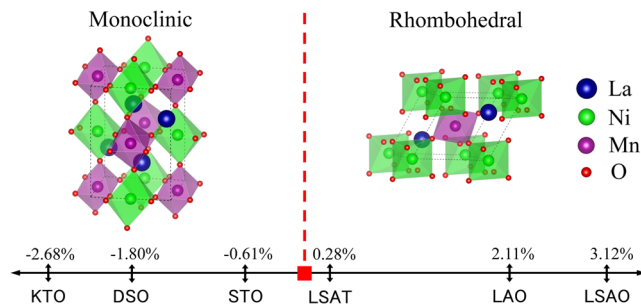
Figure 5. Epitaxial-strain-induced phase transition in LNMO films. The in-plane lattice mismatch values between LNMO and a variety of substrates are given. For monoclinic phase, the value is the minimal in-plane lattice mismatch.

Methods

LNMO thin films were deposited on STO, KTO, DSO and LAO substrates by the pulsed laser deposition (PLD) technique. A KrF excimer laser (wavelength: 248 nm) was applied for ablation of a sintered LNMO target. The film deposition conditions were held the same for all different substrates, including the substrate temperature (900 °C), oxygen pressure (250 mTorr), target-substrate distance (10 cm), laser fluence (2 J/cm^2), and repetition frequency (5 Hz).

Cross-sectional TEM specimens were prepared by conventional TEM sample preparation technique and focused ion beam (FIB) lift-out technique using an FEI Helios600i FIB/SEM system[58]. BF-TEM images and SAED patterns were acquired on a JEM 2100 microscope. Atomic-resolution HAADF imaging and EDS mapping were performed on a JEOL ARM200F microscope equipped with an aberration corrector for a probe-forming system and an Oxford X-MaxN 100TLE spectrometer, operated at 200 kV. The HAADF detector covered an angular range of 90–176 mrad and the convergence semi-angle was set to 22 mrad for HAADF imaging.

References

1. Rogado, N. S., Li, J., Sleight, A. W. & Subramanian, M. A. Magnetocapacitance and magnetoresistance near room temperature in a ferromagnetic semiconductor: La$_2$NiMnO$_6$. *Adv. Mater.* **17**, 2225–2227 (2005).
2. Tirmali, P. M., Mane, S. M., Patil, S. K. & Kulkarni, S. B. Effects of partial site substitution on magnetic and dielectric behavior of La$_2$NiMnO$_6$ double perovskite. *J. Mater. Sci. - Mater. Electron.* **27**, 4314–4320 (2016).
3. Takahashi, R. *et al*. A site driven ferroelectricity in strained ferromagnetic La$_2$NiMnO$_6$ thin films. *Phys. Rev. B.* **91**, 134107 (2015).
4. Cao, Z. Z. *et al*. Extrinsic and intrinsic contributions for dielectric behavior of La$_2$NiMnO$_6$ ceramic. *Physica B.* **477**, 8–13 (2015).
5. Lin, Y. Q., Wu, S. Y. & Chen, X. M. Effects of ordering domain structure on dielectric properties of double perovskite La$_2$NiMnO$_6$. *J Adv Dielectr.* **01**, 319–324 (2011).
6. Dass, R. I., Yan, J. Q. & Goodenough, J. B. Oxygen stoichiometry, ferromagnetism, and transport properties of La$_{2-x}$NiMnO$_{6+\delta}$. *Phys. Rev. B.* **68**, 064415 (2003).
7. Kitamura, M. *et al*. Ferromagnetic properties of epitaxial La$_2$NiMnO$_6$ thin films grown by pulsed laser deposition. *Appl. Phys. Lett.* **94**, 132506 (2009).
8. Ullah, M. *et al*. Electronic, thermoelectric and magnetic properties of La$_2$NiMnO$_6$ and La$_2$CoMnO$_6$. *J. Magn. Magn. Mater.* **377**, 197–203 (2015).
9. Truong, K. D., Singh, M. P., Jandl, S. & Fournier, P. Influence of Ni/Mn cation order on the spin-phonon coupling in multifunctional La$_2$NiMnO$_6$ epitaxial films by polarized Raman spectroscopy. *Phys. Rev. B.* **80**, 134424 (2009).
10. Singh, M. P. *et al*. Absence of long-range Ni/Mn ordering in ferromagnetic La$_2$NiMnO$_6$ thin films. *Appl. Phys. Lett.* **91**, 012503 (2007).
11. Vasala, S. & Karppinen, M. A$_2$B′B″O$_6$ perovskites: A review. *Prog. Solid State Chem.* **43**, 1–36 (2015).
12. Blasse, G. Ferromagnetic interactions in non-metallic perovskites. *J. Phys. Chem. Solids.* **26**, 1969–1971 (1965).
13. Wold, A., Arnott, R. J. & Goodenough, J. B. Some magnetic and crystallographic properties of the system LaMn$_{1-x}$Ni$_x$O$_{3+\lambda}$. *J. Appl. Phys.* **29**, 387–389 (1958).
14. Joly, V. L. J., Joy, P. A., Date, S. K. & Gopinath, C. S. Two ferromagnetic phases with different spin states of Mn and Ni in LaMn$_{0.5}$Ni$_{0.5}$O$_3$. *Phys. Rev. B.* **65**, 184416 (2002).
15. Choudhury, D. *et al*. Near room temperature colossal magnetodielectricity and multiglass properties in partially disordered La$_2$NiMnO$_6$. *Phys. Rev. Lett.* **108**, 127201 (2012).
16. Blasco, J. *et al*. Magnetic properties of LaNi$_{1-x}$Mn$_x$O$_{3+\delta}$ perovskites. *Eur. Phys. J. B.* **30**, 469–479 (2002).
17. Blasco, J., Sanchez, M. C., Perez-Cacho, J. & Campo, J. Synthesis and structural study of LaNi$_{1-x}$Mn$_x$O$_{3+\delta}$ perovskites. *J. Phys. Chem. Solids.* **63**, 781–792 (2002).
18. Devi Chandrasekhar, K., Das, A. K., Mitra, C. & Venimadhav, A. The extrinsic origin of the magnetodielectric effect in the double perovskite La$_2$NiMnO$_6$. *J Phys Condens Matter.* **24**, 495901 (2012).
19. Hashisaka, M. *et al*. Epitaxial growth of ferromagnetic La$_2$NiMnO$_6$ with ordered double-perovskite structure. *Appl. Phys. Lett.* **89**, 032504 (2006).
20. Sakurai, Y., Ohkubo, I., Matsumoto, Y., Koinuma, H. & Oshima, M. Influence of substrates on epitaxial growth of B-site-ordered perovskite La$_2$NiMnO$_6$ thin films. *J. Appl. Phys.* **110**, 063913 (2011).
21. Mi, S. B. *et al*. Heterostructures of BaTiO$_3$ bilayer films grown on SrTiO$_3$ (001) under different oxygen pressures. *J. Cryst. Growth.* **283**, 425–430 (2005).
22. Jing, H. M. *et al*. Microstructure and electrical conductivity of (Y, Sr)CoO$_{3-\delta}$ thin films tuned by the film growth temperature. *J. Alloys Compd.* **714**, 181–185 (2017).
23. Singh, M. P., Charpentier, S., Truong, K. D. & Fournier, P. Evidence of bidomain structure in double-perovskite La$_2$CoMnO$_6$ thin films. *Appl. Phys. Lett.* **90**, 211915 (2007).

24. Singh, M. P., Truong, K. D., Jandl, S. & Fournier, P. Long-range Ni/Mn structural order in epitaxial double perovskite La_2NiMnO_6 thin films. *Phys. Rev. B.* **79**, 224421 (2009).

25. Masuno, A. *et al.* Epitaxial growth and B-site cation ordering in layered double perovskite La_2CuSnO_6 thin films. *Appl. Phys. Lett.* **89**, 211913 (2006).

26. Jin, X. W., Lu, L., Mi, S. B., Liu, M. & Jia, C. L. Phase stability and B-site ordering in La_2NiMnO_6 thin films. *Appl. Phys. Lett.* **109**, 031904 (2016).

27. Xie, C. Z. & Shi, L. Tuning of magnetic properties for epitaxial Y_2NiMnO_6 thin film: Substrate is crucial. *Appl. Surf. Sci.* **384**, 459–465 (2016).

28. Zeches, R. J. *et al.* A strain-driven morphotropic phase boundary in $BiFeO_3$. *Science.* **326**, 977–980 (2009).

29. Dixit, H. *et al.* Understanding strain induced phase transformations in $BiFeO_3$ thin films. *Adv Sci (Weinh).* **2**, 1500041 (2015).

30. Du, C. *et al.* Control of magnetocrystalline anisotropy by epitaxial strain in double perovskite Sr_2FeMoO_6 films. *Phys. Rev. Lett.* **110**, 147204 (2013).

31. Infante, I. C. *et al.* Bridging multiferroic phase transitions by epitaxial strain in $BiFeO_3$. *Phys. Rev. Lett.* **105**, 057601 (2010).

32. Zhou, X. L., Stern, I., Silwal, P., Miao, L. D. & Ho Kim, D. Coherent in-plane tensile strain in perovskite $Ba_{0.8}Sr_{0.2}TiO_3$ films on spinel $MgAl_2O_4$ substrates. *Appl. Phys. Lett.* **100**, 032902 (2012).

33. Dupé, B. *et al.* Competing phases in $BiFeO_3$ thin films under compressive epitaxial strain. *Phys. Rev. B.* **81**, 144128 (2010).

34. Hatt, A. J., Spaldin, N. A. & Ederer, C. Strain-induced isosymmetric phase transition in $BiFeO_3$. *Phys. Rev. B.* **81**, 054109 (2010).

35. Mix, C. & Jakob, G. Multiferroic and structural properties of $BiFeO_3$ close to the strain induced phase transition on different substrates. *J. Appl. Phys.* **113**, 17D907 (2013).

36. Goodenough, J. B., Wold, A., Arnott, R. J. & Menyuk, N. Relationship between crystal symmetry and magnetic properties of ionic compounds containing Mn^{3+}. *Phys. Rev.* **124**, 373–384 (1961).

37. Sayed, F. N. *et al.* Role of annealing conditions on the ferromagnetic and dielectric properties of La_2NiMnO_6. *J. Mater. Res.* **26**, 567–577 (2011).

38. Jia, C. L., Lentzen, M. & Urban, K. Atomic-resolution imaging of oxygen in perovskite ceramics. *Science.* **299**, 870–873 (2003).

39. Jia, C. L. & Urban, K. Atomic-resolution measurement of oxygen concentration in oxide materials. *Science.* **303**, 2001–2004 (2004).

40. Jia, C. L., Urban, K. W., Alexe, M., Hesse, D. & Vrejoiu, I. Direct observation of continuous electric dipole rotation in flux-closure domains in ferroelectric $Pb(Zr,Ti)O_3$. *Science.* **331**, 1420–1423 (2011).

41. Pennycook, T. J. *et al.* 3D elemental mapping with nanometer scale depth resolution via electron optical sectioning. *Ultramicroscopy.* **174**, 27–34 (2017).

42. Gázquez, J. *et al.* Applications of STEM-EELS to complex oxides. *Mater. Sci. Semicond. Process.* **65**, 49–63 (2017).

43. Mi, S. B., Jia, C. L., Vrejoiu, I., Alexe, M. & Hesse, D. Atomic-scale structure and properties of epitaxial $PbZr_{0.2}Ti_{0.8}O_3/SrRuO_3$ heterointerfaces. *Adv. Mater. Interfaces.* **2**, 1500087 (2015).

44. Findlay, S. D. *et al.* Robust atomic resolution imaging of light elements using scanning transmission electron microscopy. *Appl. Phys. Lett.* **95**, 191913 (2009).

45. Howard, S. A., Yau, J. K. & Anderson, H. U. Structural characteristics of $Sr_{1-x}La_xTi_{3\pm\delta}$ as a function of oxygen partial pressure at 1400 °C. *J. Appl. Phys.* **65**, 1492–1498 (1989).

46. Zhurova, E. A., Ivanov, Y., Zavodnik, V. & Tsirelson, V. Electron density and atomic displacements in $KTaO_3$. *Acta Cryst.* **B56**, 594–600 (2000).

47. Hayward, S. A. *et al.* Transformation processes in $LaAlO_3$: Neutron diffraction, dielectric, thermal, optical, and Raman studies. *Phys. Rev. B.* **72**, (2005).

48. Liferovich, R. P. & Mitchell, R. H. A structural study of ternary lanthanide orthoscandate perovskites. *J. Solid State Chem.* **177**, 2188–2197 (2004).

49. Nellist, P. D. *et al.* Aberration-corrected STEM: current performance and future directions. *J. Phys.* **26**, 7–12 (2006).

50. Jin, L., Jia, C. L. & Vrejoiu, I. Engineering 180° ferroelectric domains in epitaxial $PbTiO_3$ thin films by varying the thickness of the underlying $(La,Sr)MnO_3$ layer. *Appl. Phys. Lett.* **105**, 132903 (2014).

51. Du, H. C. *et al.* Atomic structure of antiphase nanodomains in Fe-doped $SrTiO_3$ films. *Adv. Funct. Mater.* **25**, 6369–6373 (2015).

52. Bull, C. L., Gleeson, D. & Knight, K. S. Determination of B-site ordering and structural transformations in the mixed transition metal perovskites La_2CoMnO_6 and La_2NiMnO_6. *J. Phys.: Condens. Matter.* **15**, 4927–4936 (2003).

53. Pawlak, D. A. *et al.* Structure and spectroscopic properties of $(AA')(BB')O_3$ mixed-perovskite crystals. *J. Mater. Res.* **20**, 3329–3337 (2011).

54. Magrez, A. *et al.* Using CBED and crystallographic image processing to evidence a structural distortion in a new family of ionic conductor $Sr_{1-x}La_{1+x}Al_{1-x}Mg_xO_4$. *J. Solid State Chem.* **172**, 243–251 (2003).

55. Borg, R. J. & Dienes, G. J. An introduction to solid state diffusion. Academic press. (1988).

56. Yang, X. *et al.* Two-step sintering: An approach to prepare $Ba(Zn_{1/3}Nb_{2/3})O_3$ ceramics with high degree of cation ordering. *J. Alloys Compd.* **723**, 930–935 (2017).

57. Kaczmarek, S. E. & Thornton, B. P. The effect of temperature on stoichiometry, cation ordering, and reaction rate in high-temperature dolomitization experiments. *Chem. Geol.* **468**, 32–41 (2017).

58. Jin, X. W. *et al.* Atomic scale investigation of planar defects in $0.95Na_{0.5}Bi_{0.5}TiO_3$–$0.05BaTiO_3$ thin films on $SrTiO_3$ (001) substrates. *J. Alloys Compd.* **676**, 173–180 (2016).

Acknowledgements

Author Contributions

S.B.M. supervised this work. S.C. and M.L. prepared thin films. L.L. prepared (S)TEM specimens. S.Q.W., S.D.C., X.W.J. and S.B.M. conducted (S)TEM investigations. S.B.M. and S.Q.W. analyzed the results and wrote the manuscript. All authors reviewed the manuscript.

Additional Information

Supplementary information accompanies this paper at https://doi.org/10.1038/s41598-018-20812-4.

Competing Interests: The authors declare no competing interests.